ORIGINAL PAPER

Oscillations and Synchrony in Large-scale Cortical Network Models

Nikolai F. Rulkov · Maxim Bazhenov

Abstract Intrinsic neuronal and circuit properties control the responses of large ensembles of neurons by creating spatiotemporal patterns of activity that are used for sensory processing, memory formation, and other cognitive tasks. The modeling of such systems requires computationally efficient single-neuron models capable of displaying realistic response properties. We developed a set of reduced models based on difference equations (map-based models) to simulate the intrinsic dynamics of biological neurons. These phenomenological models were designed to capture the main response properties of specific types of neurons while ensuring realistic model behavior across a sufficient dynamic range of inputs. This approach allows for fast simulations and efficient parameter space analysis of networks containing hundreds of thousands of neurons of different types using a conventional workstation. Drawing on results obtained using large-scale networks of map-based neurons, we discuss spatiotemporal cortical network dynamics as a function of parameters that affect synaptic interactions and intrinsic states of the neurons.

Keywords Neuron · Cortical network · Large-scale model · Gamma oscillations

1 Introduction

The most realistic approach for simulation of neuronal behavior is based on Hodgkin–Huxley-type models [1] where each ionic current is described using voltage-dependent opening and closing rates for the gating variables. Examples of successful Hodgkin–Huxley-type models include cortical cells [2–6], thalamic relays [7–9], reticular cells [10–12], hippocampal neurons [13, 14], and antennal lobe neurons [15, 16], among others.

N. F. Rulkov (✉)
UCSD and Information Systems Labs. Inc., San Diego, CA, USA
e-mail: nrulkov@ucsd.edu

M. Bazhenov
The Salk Institute, San Diego, CA, USA

Unfortunately, the high dimensionality and complexity of nonlinear functions that constitute Hodgkin–Huxley-type models hamper their application to the simulation of large-scale networks containing a realistic number of neurons.

Integrate and fire models (IF) [17–19] are a class of models commonly used in large-scale simulations. In the IF model, a neuron simply integrates its inputs and generates a spike when a threshold is reached. After the spike, the membrane voltage is reset to zero, followed by a refractory period during which spiking is impossible. The disadvantage of IF models is that the firing patterns are oversimplified and do not describe the range of experimental data. IF models also fail to reproduce nonlinear intrinsic resonance properties of biological neurons. Generalizations of this simple model include leaky IF models that introduce a leak term in the dynamics of the subthreshold membrane voltage and the integrate-and-fire-or-burst neuron model that reproduces rebound bursting observed in some cell types [20, 21]. However, generalizations of the IF model that help describe realistic firing patterns significantly increase the complexity of the IF-based model and reduce the speed of computer simulations. One recent exception proposed by Izhikevich [22] is designed in the form of a two-dimensional system of ordinary differential equations that replicates a variety of physiological firing patterns. For computer simulations, this model was rewritten as a system of difference equations using Euler's integration scheme with a step size small enough to allow the resolution of spikes.

We have proposed a way to improve the computational efficiency of network simulations by designing a model of spiking neurons that neglects the duration and shape of individual spikes but captures the dynamics occurring over other time scales [23–25]. This is achieved by designing the dynamical system in the form of difference equations (i.e., a map). The explicit discretization in time permits a relatively low sampling rate of 0.5 ms, enabling efficient simulation. However, in contrast to continuous time models simulated at a low sampling rate, each spike is given by a single sample in the waveform data and is, therefore, never missed. In addition to the firing patten, other relatively slow dynamical processes are captured correctly by the map-based model because they are unaffected by the temporal discreteness of the model. Attractive features of this map-based model include the simplicity of the equations, the ability to describe a broad range of firing patterns found in biological neurons, and the opportunity to adopt models of synaptic inputs used in simulations of networks with Hodgkin–Huxley equations.

In this paper, we start by introducing the map-based model. The dynamics is discussed as a function of the model parameters. In the second part of the manuscript, we use this generic approach to design specific models describing different classes of thalamic and cortical neurons that are analyzed in response to constant and periodic external inputs. In the last section, we apply this approach to study intrinsic mechanisms and synchronization properties of fast gamma-range (30–80 Hz) oscillations in large-scale, two-dimensional cortical network models.

2 Map-based Approach to Modeling a Typical Action Potential

An action potential (spike) represents one of the best known characteristic features of biological neurons and plays an important role in information transfer across neuronal systems. In many classes of biological neurons, action potentials are generated by the dynamics of voltage-dependent Na^+ and K^+ conductances [1]. In this section, we will introduce a reduced model of a biological neuron that simulates action potential generation.

The waveform of the action potential can be replicated using the reduced model written in the form of a one-dimensional nonlinear difference equation (map) as follows:

$$x_{n+1} = f_\alpha(x_n, u_n). \tag{1}$$

Here, the dynamical variable x_n represents the membrane potential of a biological neuron. It samples the action potential waveform at the discrete moments of time n.[1] The time-dependent variable $u_n = y + \beta_n$ includes two components: the parameter y defines the baseline (resting potential) of the neuron and the time-dependent term, β_n (index n indicates value of β at time n), represents the external input to the model (e.g., external and synaptic currents).

The shape of each spike of neuronal activity is replicated here using a piece-wise nonlinear function $f_\alpha(x_n, u_n)$ suggested in [24]:

$$f_\alpha(x_n, u_n) = \begin{cases} \alpha/(1 - x_n) + u_n, & x_n \leq 0 \\ \alpha + u_n, & 0 < x_n < \alpha + u_n \text{ and } x_{n-1} \leq 0 \\ -1, & x_n \geq \alpha + u_n \text{ or } x_{n-1} > 0. \end{cases} \tag{2}$$

The control parameter α in (1) is usually selected from the range $3 < \alpha < 4$ for tonically spiking (nonbursting) neurons (see more about this below). The nonlinear interval of the function at negative values of x_n replicates the subthreshold state of a neuron (e.g., the phase of the resting potential, stimulation, and the rising phase of a spike). The other two conditions of (2) are involved in shaping the tip of the spike (made by a single sample at $x_n = \alpha + u_n$) followed by repolarization, which is done here with one iteration of the map. In analogy with conductance-based models, these two intervals represent the activation of the voltage-dependent Na^+ and K^+ conductances. Note that, though the main part of the map (i.e., the interval $x_n \leq 0$) is a one-dimensional map, the condition for repolarization requires the use of x_{n-1}. These values ensure the stability of the repolarization phase in the presence of external stimuli applied to the model (see [24] for details).

The model (1) exhibits two main dynamic states of a biological neuron, a silent state and a periodic sequence of action potentials. Indeed, depending on the values of y (assuming that $\beta_n = 0$) (1), the map may have a pair of fixed points x_{ps}, x_{pu} and a limit cycle (see [24] for details). The stable fixed point $x_{ps} = F(\alpha, u_n)$ represents the resting state, and the limit cycle, a spike sequence. Remember that the variable u_n includes a time-dependent component β_n representing input to the system. When a stimulus (e.g., an external or synaptic current) is applied to (1), β_n becomes zero. If $\beta_n > 0$ becomes large enough, the x_{ps} and x_{pu} merge and disappear, triggering the rising phase of a spike. The value of the variable x_n where the fixed points merge is given by $x_{th} = 1 - \sqrt{\alpha}$. The corresponding value of u_n is given by $u_{th} = 1 - 2\sqrt{\alpha}$. Thus, like conductance-based models, neurons that are more depolarized at rest (large values of y) require less external input (β_n) to reach the threshold for spike generation.

Since (1) is written in a dimensionless form, it generates waveforms with x_n values ranging from -2 to 2. To recalibrate the waveforms of the map to millivolts, allowing

---

[1]More often than not, neuronal dynamics is simulated using differential equations rather than difference equations (for example, the Hodgkin–Huxley model [1], the IF model [17–19], and the Izhikevich model [22]). However, it is important to emphasize that to solve a differential equation numerically, it is usually rewritten in the form of a difference equation (e.g., using the Euler scheme, the time derivative dV/dt is replaced by $(V_{n+1} - V_n)/\tau$).

a comparison with Hodgkin–Huxley models or with experimental data, one can use the following relationship:

$$v_n[\text{mV}] = \frac{-50\,\text{mV}}{1 - \sqrt{\alpha}} \times x_n, \tag{3}$$

where the denominator stands for the triggering state that typically occurs at a depolarization level near -50 mV. This normalization sets the peak of the spike that occurs at $x_n = \alpha + u_{\text{th}} = (1 - \sqrt{\alpha})^2$, to $50\,\text{mV}(\sqrt{\alpha} - 1)$, which reaches 50 mV for the case $\alpha = 4$.

Thus far, we discussed the model with no explicit time scale. Again, using an analogy with Euler's method of approximating a differential equation, the time interval between two successful iterations of the map (1) is set to be equal to the numerical integration time step. However, since the model (1) is introduced as a difference equation, we need to specify the time scale. This can be done using width of a sodium spike that is constrained by the kinetics of Na^+ and K^+ conductances and typically falls between 1 and 2 ms (at half amplitude). Based on this information, we can set the time interval between iterations of a map (1) as 0.5 ms.

3 Slow Dynamics in the Map-based Model of Neurons

The model (1) introduced in the previous section is capable of a transition between silence and tonic spiking. To introduce more complex dynamics, including spike adaptation or bursting, we need to introduce a slow dynamical variable, which may also be described by a difference equation. In this section, we consider an approach that replicates the slow oscillatory properties of a neuron. This approach, suggested in [24], consists of a map-based model that is capable of generating various types of spiking and spiking–bursting activity. The system including additional slow dynamics may be written as follows:

$$x_{n+1} = f_\alpha(x_n, y_n + \beta_n),$$
$$y_{n+1} = y_n - \mu(x_n + 1) + \mu\sigma + \mu\sigma_n, \tag{4}$$

where x_n is the fast and y_n is the slow dynamical variable. The slow time evolution of y_n is achieved by using small values of the parameter $\mu << 1$. Here, the control parameter y used in (1) as the last argument of the function f_α is substituted with a slow variable y_n. Input variables β_n and σ_n introduce the action of synaptic current I^{syn} and other external currents injected into the neuron. The parameter σ defines the resting potential of the model neuron.

Detailed analysis of the individual dynamics of model (4), with $\beta_n = 0$ and $\sigma_n = 0$, as a function of the control parameters σ and α, was done in [24, 26]. In the two-dimensional map-based model, the single fixed point O_0 defines the resting potential level, which is now set using the control parameter σ instead of y, used in (1). When $\sigma < \sigma_{\text{th}} = 2 - \sqrt{\alpha/(1 - \mu)}$, the system converges to a stable fixed point O_0 with coordinates $x_0 = -1 + \sigma$ and $y_0 = -1 + \sigma - \alpha/(2 - \sigma)$, and the neuron stays silent. At the threshold $\sigma = \sigma_{\text{th}}$, the fixed point loses stability due to a subcritical Neimark–Sacker bifurcation (see, for example, [27]) and, for $\sigma > \sigma_{\text{th}}$, the map generates spikes.[2] Note that the value of x_n

---

[2]One can simplify the condition for the threshold by introducing a new control parameter $\sigma^{\text{new}} = \sigma - 2 + \sqrt{\alpha/(1 - \mu)}$. In this case, the threshold value occurs at $\sigma_{\text{th}}^{\text{new}} = 0$. In this paper, we do not use this change of the control parameter.

corresponding to the threshold level fixed point is $x_{\text{th}} = 1 - \sqrt{\alpha(1-\mu)} \approx 1 - \sqrt{\alpha}$, which is about the same as in the model (1) and, therefore, normalization (3) remains valid for this case.

We would like to emphasize that the addition of the slow variable y_n to the model (1) resulted in a change in the type of neuronal excitability. The case (1) describes a type-1 neuron where the transition from silence to spiking occurs via a saddle-node bifurcation. The map (4) describes a type-2 neuron where the transition to spiking occurs via an Andronov–Hopf bifurcation. The details of this classification may be found elsewhere [28].

The bifurcation diagram of the map (4) plotted in the parameter plane (σ, α) is presented in Fig. 1. The diagram shows the parameter regions corresponding to three regimes of behavior: silence, continuous spiking, and generation of the bursts of spikes. Near the border between the spiking and spiking–bursting activity, shown by curve L_{ts}, there exists a parameter domain, outlined by dashed lines, where chaotic regimes of continuous spiking and the bursting activity occur; see [26] for details.

The diagram also shows that the parameter σ simulates the effect of a depolarizing current injected into the real neuron [29]. To get a better view of this similarity, consider the reaction of the map to a slowly increasing value of σ. The test with a slow ramp of injected current is frequently used in biological experiments. The plots of the map reaction obtained in this test with a slew rate $\Delta\sigma = 0.00005$ per iteration are presented in Fig. 2. The two top panels of this figure illustrate a transition from silence to spiking through the phase of spiking bursting activity. The transition from silence to continuous spiking without bursting, which takes place for $\alpha \leq 4.0$, is shown in Fig. 2c. Qualitatively different transitions (compare Fig. 2c with Fig. 2a and b) produced by the model are observed in real neurons; see, for example, the responses of the PD and GM neurons of the stomatogastric ganglion of the Californian lobster to a depolarizing ramp current [30].

Notice that, due to a continuous increase in the value of parameter σ, the oscillations in the map occur later then one would expect based on the threshold values σ_{th} given in

Fig. 1 Diagram of dynamical regimes produced by map (4). Irregular (chaotic) spiking and spiking–bursting oscillations are typical within the intermediate region outlined by *dashed lines* and σ_{th}
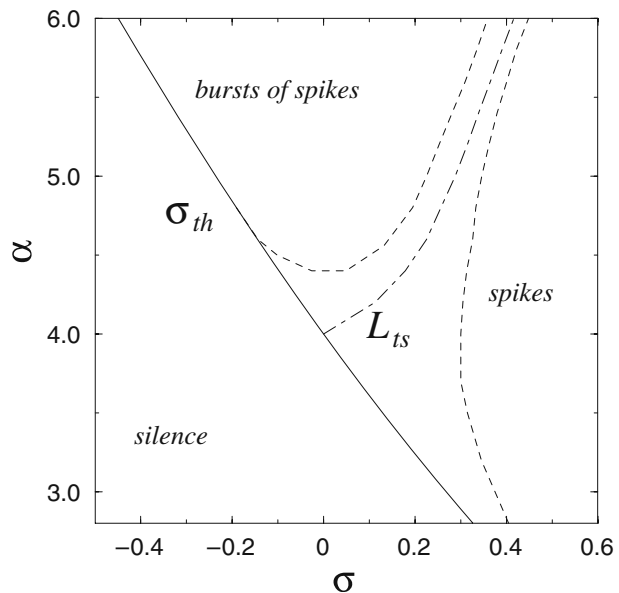
Fig. 2 Restructuring of oscillation in map (4) with **a** α=5.0, **b** α=4.5, and **c** α=4.0, as the value of σ increases with the constant slew rate $\Delta\sigma = 0.00005$ per iteration
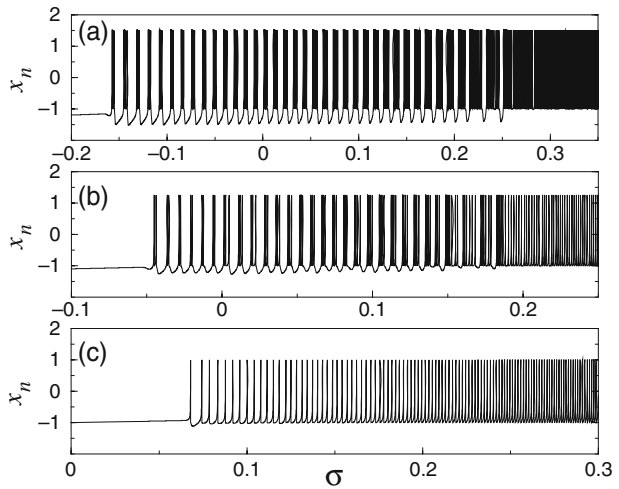

Fig. 1. Usually, spiking in biological neurons occurs more readily for fast increases in the depolarization current than for the slow ones. A method to obtain realistic responses from the map (4) to the dynamically changing input currents is discussed in the next section, where we will describe the effects of injecting a current I_n using input variables β_n and σ_n. Note that σ_n in (4) adds to parameter σ and, therefore, acts similarly.

3.1 Modeling the Response to Input Currents

Inputs to the model (4) are described by two variables, β_n and σ_n, that are functions of external (e.g., synaptic or any other) currents. σ_n acts through the slow subsystem of (4). It changes the location of the fixed point O and the system responds to it by slowly moving towards a new state. Changes of the value of β_n, on the contrary, act instantly through the fast subsystem of (4) and quickly change the state of the neuron. However, after the changes in β_n, the system (4) slowly drifts towards the original dynamics. Using the change of the slow variable in (4), one can combine both these input parameters and rewrite (4) in the form

$$x_{n+1} = f(x_n, u_n),$$
$$u_{n+1} = u_n - \mu(x_n + 1) + \mu\sigma + \eta_n,$$

where $u_n = y_n + \beta_n$ is the new variable and $\eta_n = \mu\sigma_n - \beta_{n+1} + \beta_n$ is the new input parameter. Here, one can see that the map reacts only to the changes (derivative) in β_n, while the absolute value of the β_n does not affect the transient dynamics of the map.

In practice, it is convenient to use the system in the form (4). Both variables β_n and σ_n are useful in modeling a variety of response dynamics. In constructing a model that mimics the response of a real biological neuron, one should experiment with the map and define a proper balance between these two functions of external current to achieve the best match between the response of the model and the neuron under study. Some approaches and ideas of modeling with map (4) are discussed later in this section.

Before considering possible models for synaptic coupling among map-based neurons, let us examine the response of the map to a rectangular pulse of external current $I^{\text{ext}}(t)$.

This would correspond to experiments with direct current injection through a sharp microelectrode. A pulse of current, in the model, may be presented by $I_n^{ext} = I^{ext}(nT)$, where T is the period of sampling (0.5 ms). The inputs β_n and σ_n can, in general, be selected as nonlinear functions of I_n^{ext} or be controlled dynamically by I_n^{ext} with a set of difference equations.

### 3.2 Effect of Model Parameters: Linear Dependence on Input Current

Let us first consider the simplest case when β_n and σ_n are linear functions of the external current,

$$\beta_n = \beta^e I_n^{ext}, \quad \sigma_n = \sigma^e I_n^{ext}, \tag{5}$$

where the constants β^e and σ^e are used to adjust the balance between the two input variables. The responses generated by the map for different values of the pulse amplitude I_a and parameter β^e are shown in Fig. 3. The parameters of the map are selected such that the neuron is in the silent regime: $\alpha = 4.0$ and $\sigma = -0.4$. The waveforms are computed for the case when the value of I_n^{ext} changes from zero in the initial state to $I_n^{ext} = I_a$ at time $n = 3{,}000$. After 1,000 iterations (≈ 0.5 s), the value of I_n^{ext} returns back to zero. The value of σ^e is set to one. The left panels illustrate changes in the response as a function of the pulse amplitude I_a with fixed β^e. The right panels illustrate the influence of the value of β^e on the response behavior when the amplitude of current pulse is fixed to $I_a = 0.45$.

The dynamical mechanisms behind the neuron model's responses shown in Fig. 3 are clear from the phase portraits presented in Fig. 4, where the curves S_s and S_u correspond to the stable and unstable branches of the slow manifolds in the limit $\mu \to 0$. The fixed point, O, of the map (4) is located at the intersection of these curves with the y-equilibrium line $x = \sigma - 1$. When $\sigma_n = 0$, the system stays in the stable fixed point O shown by the open circle on the stable branch S_s. When a depolarizing pulse is applied, the y-equilibrium line shifts up by the distance $D = \sigma_n$ and, as a result, the location of O on the slow manifold

Fig. 3 Waveforms of x_n for the responses of map (4) to a rectangular pulse of amplitude I_a and duration 1,000 iterations computed for different pulse amplitudes (*left*) and the input balance parameter β^e (*right*). The shapes of the pulse are shown below the traces of x_n. The parameter values are $\alpha = 4.0$, $\sigma = -0.4$, $\sigma^e = 1.0$, and
a - $I_a = 0.630$, $\beta^e = 0.224$;
b - $I_a = 0.517$, $\beta^e = 0.224$;
c - $I_a = 0.439$, $\beta^e = 0.224$;
d - $I_a = 0.394$, $\beta^e = 0.224$;
e - $\beta^e = 0.3$, $I_a = 0.45$;
f - $\beta^e = 0.2$, $I_a = 0.45$;
g - $\beta^e = 0.1$, $I_a = 0.45$;
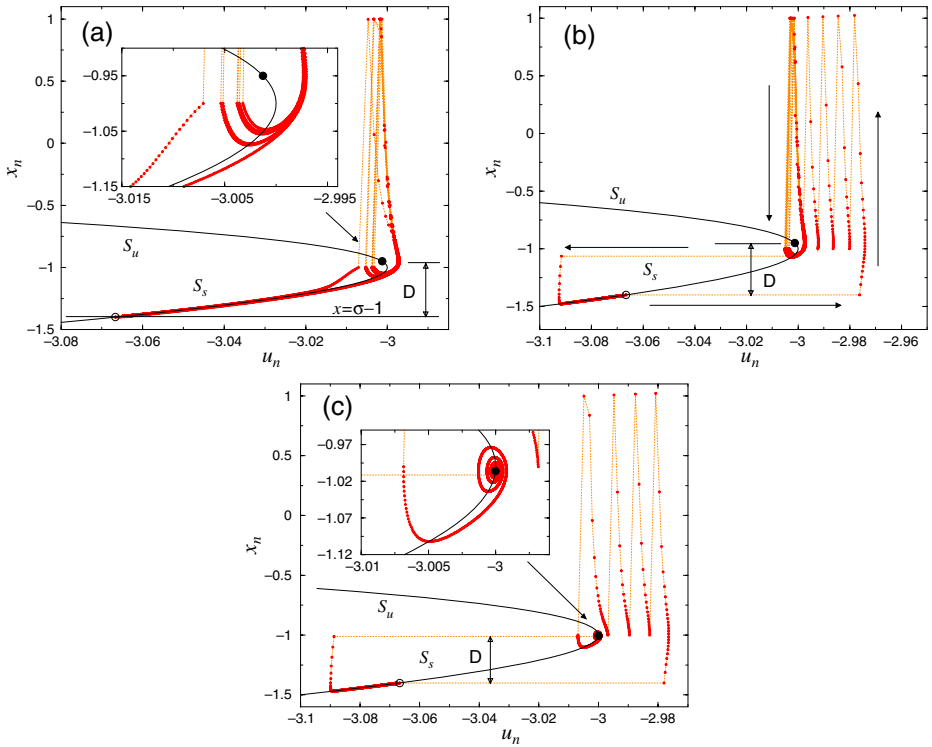**h** - $\beta^e = 0.0$, $I_a = 0.45$
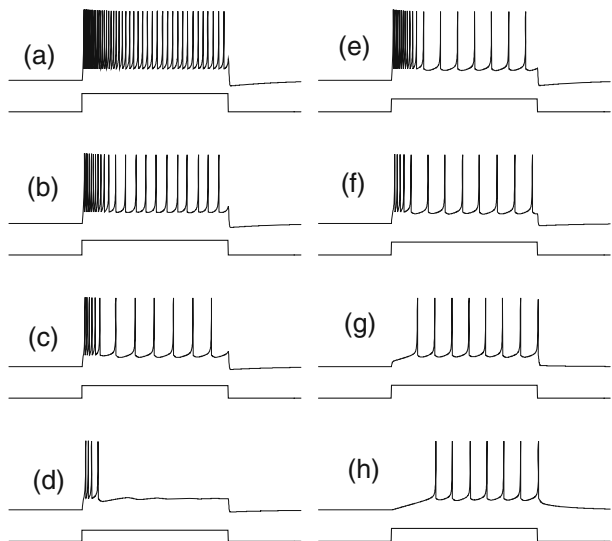
Fig. 4 Phase portraits of the map (4) in the plane of variables $u_n = y_n + \beta_n$ and x_n explaining the dynamical mechanisms behind the main properties of waveforms for the responses shown in Fig. 3. The samples generated by the map-based model are shown with *red dots*. To follow the trajectory of the map, these dots are connected with *straight yellow lines*. **a**, **b**, and **c** Phase portraits for the trajectories shown in Fig. 3h, f, and d, respectively

changes. The location of O during a pulse of current is shown in Fig. 4 by the black filled circle. When $\beta^e = 0$, the trajectory of the system moves from the initial equilibrium state towards the new one along the manifold. If the perturbed fixed point in the new state is unstable (i.e., located in the branch S_u), then the map generates spikes; see Fig. 4a. After the pulse ends, the system returns to the original state. The corresponding waveform is shown in Fig. 3h.

The presence of the input function β_n in the first equation (4) dramatically changes the transient dynamics of the map; see Fig. 4b and c. This effect is easy to analyze using the phase plane (u_n, x_n) instead of (y_n, x_n). In the case of nonzero β^e, the pulse of current makes the trajectory jump parallel to axis u_n over a distance $\beta^e I_a$. As a result, after one iteration, the trajectory gets far into the spiking regime, following which the system slowly approaches the new state, a periodic motion, in the case shown in Fig. 4b, or a stable equilibrium, Fig. 4c. When the pulse of current turns off, the trajectory jumps back parallel to axis u_n. It may overshoot the original state (resting potential) and, as a result, some time is needed before the system returns to it, sliding along the stable branch S_s.

One of the characteristics of the neuronal response patterns that can be tested in biological experiments is the time-dependence of the frequency of spiking f_S and the variation

Fig. 5 The plots of f_s vs n computed for the waveforms shown in Fig. 3a, b, c, and d.
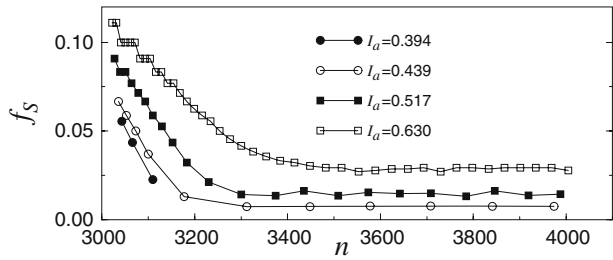
of this dependence with the amplitude of the depolarizing pulse [31]. This dependence, computed for the waveforms shown in the left panels of Fig. 3, is presented in Fig. 5.

The role of the parameter β^e may be seen from the traces obtained for a fixed value of $I_a = 0.45$ and six different values of β^e (see Fig. 6). This parameter accelerates the firing at the beginning of the injected pulse followed by a decrease in spiking frequency down to the rate set by the input current $\sigma_n = I_a$. The rate of deceleration is controlled by the value of the parameter μ.

Following the depolarizing current pulse, β_n changes from a positive value, $\beta^e I_a$, to zero, resulting in a sharp decrease in the value x_n, known as after-hyperpolarization (see Fig. 3e, f). For a continuously spiking neuron, this effect can appear as the formation of an interval of silence after the depolarizing pulse ends (see Fig. 7a). When a hyperpolarizing pulse of current I_n^{ext} is applied to a continuously spiking neuron, the parameter β^e helps to model the following dynamics: The pulse shuts off spiking. When the pulse is switched off, the neuron immediately starts firing with a high frequency. The rate of spiking decreases, eventually converging back to normal (see Fig. 7b).

3.3 Effect of Model Parameters: Nonlinear Dependence on the Input Current

In order to obtain a more realistic response behavior for modeling a particular type of neuron, it can be useful to consider a nonlinear relation between input functions, σ_n, β_n, and the injected current I_n^{ext}. This can be especially helpful for capturing the effects of after-hyperpolarization and rebound bursts. The rest of this section illustrates briefly two approaches to the design of a dynamical dependence of the input functions on the current.

Consider a neuron demonstrating the following type of behavior: At baseline, given by the resting potential, the neuron does not fire spikes. It starts to spike tonically when a rectangular pulse of depolarizing current is applied over a limited duration. When the neuron

Fig. 6 The dependence of f_S on time n plotted for different values of β^e. The other parameters of the map are the same as in Fig. 3, right panels
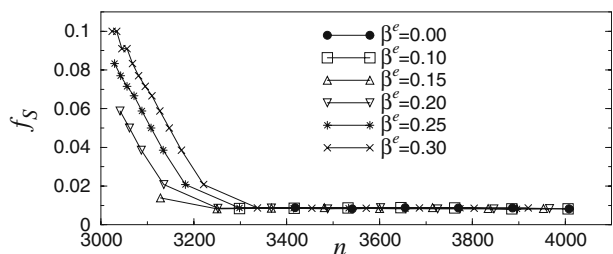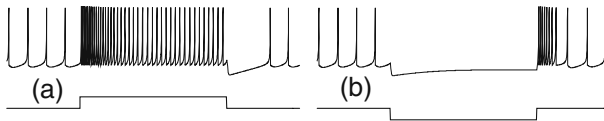
Fig. 7 The map responses to a depolarizing (**a**) and hyperpolarizing (**b**) rectangular pulse with a duration of 1,000 iterations in the case of a continuously spiking map. The parameters of the maps are $\alpha = 4.0$, $\sigma = 4.08e - 2$, and $\beta^e = 0.3$. **a** $I_a = 0.2$ and **b** $I_a = -0.2$

is driven by a slow ramp of depolarizing current, the threshold of excitation depends on the slew rate. When the slew rate is too slow, the neuron does not spike, even at levels of injected current far beyond the expected values for the spiking activity threshold. Such behavior, known as adaptation, is exhibited by the GM neuron of the stomatogastric ganglion of the Californian lobster [30]. It is clear from Fig. 1 that, if the value of σ_n is proportional to the current, the map cannot reproduce such behavior. For values of σ_n where the map crosses the threshold level σ_{th}, it starts spiking for arbitrarily low slew rates of I_n. In order to design a map that correctly models such a neuronal behavior, one can define the input function σ_n with the following equation:

$$\sigma_{n+1} = (1 - \mu_\sigma)\sigma_n + I_{n+1} - I_n,$$

where a small parameter, μ_σ ($0 < \mu_\sigma << \mu << 1$), defines the characteristic rate of adaptation of the map to slow input σ_n. In this case, the maximal value of σ_n equals $(I_{n+1} - I_n)/\mu_\sigma$. Therefore, if the parameters of the map are in the regime where the neuron is silent, at finite distance from σ_{th}, then there exists a low bound for the slew rate of the ramp of current that results in spiking.

The input function β_n may be described by a simple dynamical model used to adjust the dependence of the spike frequency f_S on the time after onset of the injected current pulse. Consider a simple example when

$$\beta_{n+1} = (1 - \mu_\beta)\beta_n + \mu_\beta \beta^e I_{n+1},$$

where parameter μ_β defines a characteristic time delay to the fast reaction of the map to the input. One can see that, when a rectangular pulse of current is applied, β_n does not change sharply but drifts towards the value $\beta^e I_{n+1}$ exponentially. As a result, the beginning of the first spike is delayed and the spiking can first accelerate and then decelerate. Numerical simulations indicate that this approach is effective only when μ_β is of the order of μ. Notice that, when $\mu_\beta = 1$, the equation for β_n transforms into the simple linear relation $\beta_n = \beta^e I_n$.

After the desired response of the map to an external current is defined, one may use well-known models for different types of synaptic currents to build a model describing a network of coupled neurons.

4 Modeling of Synaptic Inputs

With map-based models, the equation for synaptic currents can be adopted from known kinetic models, but they need to be rewritten in the form of difference equations. Examples of such equations were given in [23]. Here, we rewrite these equation in terms of synaptic conductances.

The simplest model of synaptic interaction includes a step-like change in the conductance g of the postsynaptic neuron by some fixed amount g_{syn} (maximal conductance) immediately after a presynaptic spike occurs followed by its exponential delay with a time constant τ. An equivalent map-based equation for the conductance can be written as

$$g_{n+1}^{\text{syn}} = \gamma g_n^{\text{syn}} + \begin{cases} g_{\text{syn}}, & \text{spike}_{\text{pre}}, \\ 0, & \text{otherwise,} \end{cases} \tag{6}$$

and the synaptic current is computed as

$$I_n = -g_n(x_n^{\text{post}} - x_{\text{rp}}), \tag{7}$$

where g_{syn} is the strength of the synaptic coupling and the indices pre and post stand for the presynaptic and postsynaptic variables, respectively. The first condition, "spike$_{\text{pre}}$," is satisfied when $x_n^{\text{pre}} \geq \alpha + y_n^{\text{pre}} + \beta_n^{\text{pre}}$ or $x_{n-1}^{\text{pre}} > 0$, i.e., when the value x_n^{pre} is in the rightmost interval of the function (2). It corresponds to the times when presynaptic spikes are generated. The parameter $\gamma = 1/\tau$ in (6) controls the relaxation rate of the synaptic current after the presynaptic spike is received ($0 \leq \gamma < 1$). The parameter x_{rp} defines the reversal potential and, therefore, the type of synapse: excitatory ($x_{\text{rp}} = 0$) or inhibitory ($x_{\text{rp}} = -1.1$).

To include the effects of short-term synaptic depression or facilitation, one can modify (6) by adding one more variable, d_n, that modulates the synaptic strength based on the levels of presynaptic activity. As a result, the conductance may be written in the form of a two-dimensional map,

$$\left\{ g_{n+1}^{\text{syn}}, \ d_{n+1} \right\} = \begin{cases} \left\{ \gamma g_n^{\text{syn}} + g_{\text{syn}} d_n, \ (1-\eta) d_n \right\}, & \text{spike}_{\text{pre}}, \\ \left\{ \gamma g_n^{\text{syn}}, \ 1 - (1-\varrho)(1-d_n) \right\}, & \text{otherwise,} \end{cases} \tag{8}$$

where $0 \leq \eta < 1$ set the rate of the depression and $0 < \varrho \ll 1$ controls the rate of synapse recovery. The initial conditions for (8) are $\left\{ g_0^{\text{syn}}, \ d_0 \right\} = \{0, 1\}$. As in the previous case, the synaptic current is computed using equation (7).

5 Map-based Modeling of Specific Cell Types

Different classes of biological neurons are characterized by different intrinsic firing patterns that result from a unique combination of intrinsic currents specific to a given neuron and from unique distributions of these channels across cell compartments. A common way to uncover the electrical properties of individual neurons is to study its responses to constant external inputs. In this section, we will discuss the modeling of response patterns of several major cell classes such as regular-spiking (RS), fast spiking (FS), intrinsically bursting (IB) and low-threshold spiking (LTS) neurons.

5.1 Model for RS Neuron

In [23], the model (4) was tuned to replicate firing patterns of a typical RS neuron when it spikes in response to a rectangular depolarizing pulse I_n. The input parameters, in this case, were proportional to I_n ($\beta_n = \beta^e I_n$ and $\sigma_n = \sigma^e I_n$). The parameters of the map-based model of the RS neuron were set to the following values: $\alpha = 3.65$, $\sigma = 0.06$, $\mu = 0.0005$,
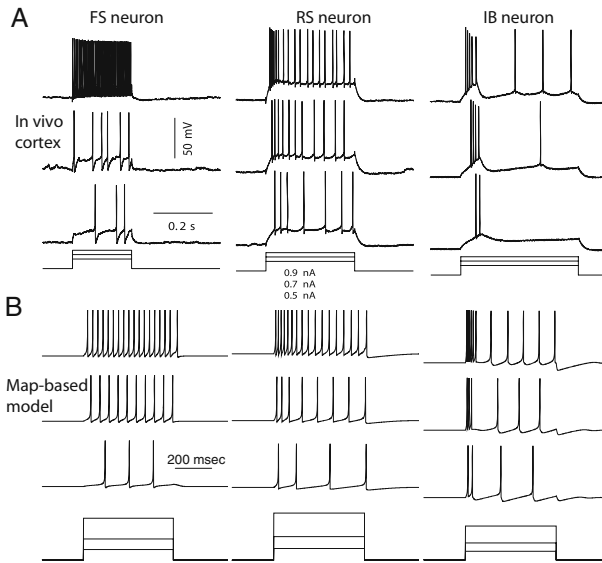
Fig. 8 Intrinsic neuronal firing patterns in vivo and in the models. **a** In vivo data. **b** Map-based model. *Left panels* show a fast spiking (*FS*) neuron, *middle panels* show a regular spiking (*RS*) neuron, and *right panel* show an intrinsically bursting (*IB*) neuron. The map-based model of the FS cell is given by (9), (10) with $\alpha = 3.8$, $y^{rs} = 2.9$, $\beta^{hp} = 0.5$, $\gamma^{hp} = 0.6$, $g^{hp} = 0.1$, $\beta^e = 0.1$, and amplitude of rectangular pulse $A = 1.6E^{-2}$ (100%). The map-based models of the RS and the IB cell are given by (4), where $\alpha = 3.65$, $\sigma = 0.06$, $\mu = 0.0005$, $\sigma^e = 1.0$, $\beta^e = 0.133$, and $A = 3.0E^{-2}$ for the RS cell, and $\alpha = 4.1$, $\sigma = -0.036$, $\mu = 0.001$, $\sigma^e = 1.0$, $\beta^e = 0.1$, and $A = 1.0E^{-2}$ for the IB cell. The duration of the depolarizing pulse in the map-based simulation is 870 iterations, which is approximately 430 ms

$\beta^e = 0.133$, and $\sigma^e = 1$. These parameter values were obtained by tuning the model to replicate the deceleration of spiking and after-hyperpolarization (Fig. 8, middle) in a Hodgkin–Huxley type model of an RS neuron. The time-rates of these effects show a strong dependence on the value of the parameter μ, while their strength may be tuned by setting the values of β^e and σ^e. The value of the parameter σ is selected to set a proper baseline of the neuron and α is tuned to match the shape of the action potential sequence. This map-based model also replicates the resonance properties of the RS neuron observed in in vivo recordings (see below and [25]).

5.2 Model for FS Interneuron

Typical firing patterns of an FS neuron in response to a rectangular pulse do not have the spike deceleration effect but shows a noticeable hyperpolarization caused by each generated spike. To capture this hyperpolarization effect, the slow subsystem in the model (4) was substituted with an equation for the hyperpolarizing current I_n^{hp} generated by the action of each spike as follows [23]:

$$I_{n+1}^{hp} = \gamma^{hp} I_n^{hp} - \begin{cases} g^{hp}, & \text{if } x_n \text{ occurs at the peak of a spike} \\ 0, & \text{otherwise.} \end{cases} \tag{9}$$

The parameter γ^{hp} controls the duration, $\tau^{hp} \sim (1 - \gamma^{hp})^{-1}$, and the parameter g^{hp} controls the amplitude of the hyperpolarization current. The model of the FS neuron in this case may be written in the following form:

$$x_{n+1} = f(x_n, x_{n-1}, y^{rs} + \beta^{hp} I_n^{hp} + \beta^e I_n), \tag{10}$$

where y^{rs} is a constant defining the resting state of the model and I_n^{hp} is a new slow variable computed using (9). Equations 9 and 10 with parameter values $\alpha=3.8$, $y^{rs} = -2.9$, $\beta^{hp} = 0.5$, $\gamma^{hp} = 0.6$, $g^{hp} = 0.1$, and $\beta^e = 0.1$ are used to describe the dynamics of an interneuron (IN) (Fig. 8, left).

5.3 Model for LTS Interneuron

Another important class of cortical interneurons – LTS interneurons – is characterized by the rebound response to a hyperpolarizing current pulse and a depolarizing sag—progressive repolarization of the cell membrane potential during hyperpolarization (see, for example, Fig. 2 in [32]). These properties are similar to the rebound response patterns found in thalamic relay and thalamic reticular neurons and have been shown to be mediated by low-threshold Ca^{2+} and hyperpolarization-activated cation (I_h) currents [33].

The map-based model is capable of replicating rebound burst generation. This is illustrated in Fig. 9, showing the waveforms generated by the map model (4) when it is hyperpolarized by a rectangular pulse of three different durations. An important feature here is that the duration of the rebound burst increases with an increase in the time over which the system is hyperpolarized. The rebound burst may be controlled by the parameter β^e and may easily be understood by an analysis of the transient behavior seen in the phase portrait in the (u_n, x_n) plane (see, for example, similar phase portraits in Fig. 4). When the values of β_n change fast from zero to a large negative value, the trajectory jumps to the left and can overshoot the new steady state. Over the duration of the hyperpolarizing pulse, the trajectory slowly approaches the new steady state and u_n and x_n slowly grow. When the hyperpolarization pulse is over the value, β_n jumps to the positive direction of u_n and the trajectory can end up in the spiking area where a burst of transient spikes can be generated.

In the model (4), the rebound response and spike adaptation are controlled by the same input parameter $\beta_n = \beta^e I_n$. Therefore, an increase in β^e will enhance both properties. To

Fig. 9 Waveforms generated by negative rectangular current pulses of amplitude 0.3 and durations of 100, 200, and 400 iterations. The beginning and end of each pulse are shown by *arrows*. Parameters of the map are $\mu = 0.002$, $\alpha = 3.8$, $\sigma - 0.15$, $\beta^e = 0.6$, and $\sigma^e = 1.0$.
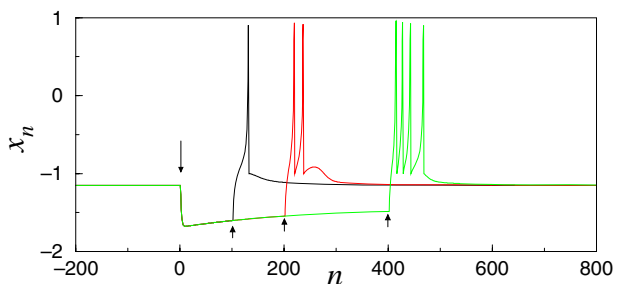
control these response features independently, we can modify the relation between β_n and I_n by making it nonlinear. For example,

$$\beta_n = \begin{cases} \beta^d I_n, & \text{if } I_n \geq 0 \\ \beta^h I_n, & \text{if } I_n < 0. \end{cases} \tag{11}$$

In this model, spike adaptation may be controlled by the parameter β^d independent of the rebound burst, which is controlled by β^h. Increasing β^h enables one to gradually enhance the rebound response to a hyperpolarizing current pulse without affecting the dynamics of the neuron in the depolarized state. Therefore, in order to build an example of a map-based model for the LTS interneuron, one may use the model (4) with the parameters of an RS cell (i.e., $\alpha = 3.65$, $\sigma = 0.06$, $\mu = 0.0005$, and $\sigma^e = 1$) and modify β_n to depend nonlinearly on the input current (11) with $\beta^d = 0.133$ and $\beta^h = 0.6$.

5.4 Model for IB Cells

IB neurons are another important class of cortical cells. They respond to depolarizing inputs with high-frequency spike bursts. In vivo, the intraburst frequency is between 4 and 10 Hz [34]. The number of spikes per burst gradually decreases over the response duration [35]. In the map-based model (4), this bursting effect is achieved by selecting the parameter α to be larger than 4, such that the model can produce bursts of spikes; see Fig. 1. Note that the number of spikes in each burst increases as the values of the parameters α and σ in the parameter region corresponding to bursting behavior increase. Figure 8, right panels, shows the response of the map-based model of the IB cell obtained using (4) with the parameter values $\alpha = 4.1$, $\sigma = -0.036$, $\mu = 0.001$, $\sigma^e = 1.0$, and $\beta^e = 0.1$.

6 Intrinsic Resonance Properties of Map-based Model Neurons

Cortical neurons display complex intrinsic resonance properties that are produced and controlled by intrinsic membrane conductances that may vary with the type of neuron. During periodic stimulation, neurons produce spikes with high reliability (across a set of trials) for stimuli within a specific frequency range. The reliability of firing diminishes at higher or lower frequencies [36, 37]. To study whether the map-based model is capable of reproducing these important properties, sine-wave modulated excitatory synaptic stimuli were applied to the map-based model of an RS neuron [25]. The amplitude of the periodic input modulation was selected such that a neuron remained silent for a constant input equal to the maximum of the sine-wave amplitude. For low modulation frequencies, both in vitro experiments and the modeled neurons produced spikes at only a few input maxima, making the reproducibility of spike trains from one trial to another low (see top panels in Fig. 10). As the input modulation frequency increased, the reliability of spiking improved. In a range of moderate frequencies (3–13 Hz), both in vitro and modeled neurons displayed almost perfect one-to-one locking with the input modulation. The origin of this resonance is subthreshold oscillations observed in real neurons [36] and captured by the dynamics of the map-based model (see [26] for details). For very high frequencies, the reproducibility of spike trains was reduced again, reflecting the inability of both in vitro and modeled neurons to follow high-frequency inputs (see bottom panel in Fig. 10). Increase of σ in (4) produced an effect similar to carbachol application in vitro—a shift of the resonance peak to a higher frequency [25].

Fig. 10 Spiking of RS neuron in response to 100 Poisson distributed independent input spike trains with sine-wave modulated mean rate: $R = f_c(1 - \sin(2 f_m t))$, where $f_c = 200$ Hz, f_m is the frequency of periodic modulation. Sampling rate: one iteration = 0.5 ms. Six different modulation frequencies f_m and 16 trials for each frequency (raster) are shown. Each *dot* represents a spike. Map-based model of RS cell (*left*) and experiment with a RS cell of rat prefrontal cortex (*right*)
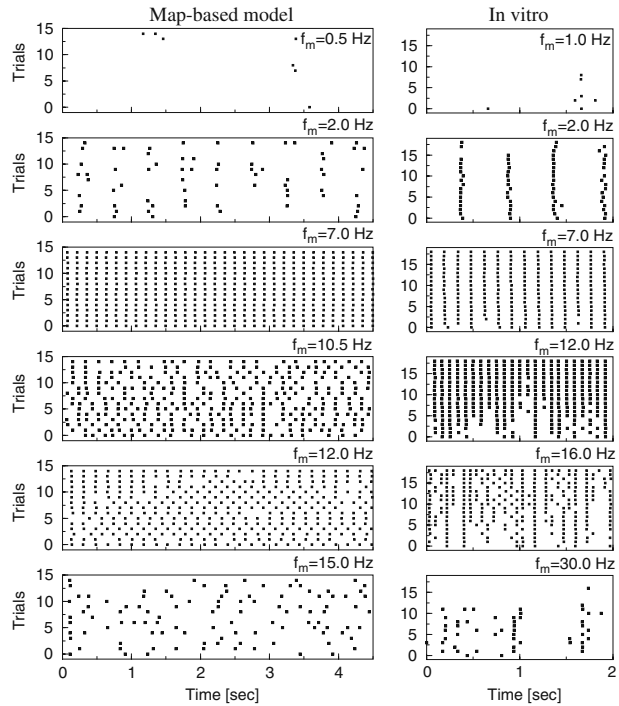
7 Oscillations in Cortical Networks

Fast network oscillations in the 30–80-Hz range are associated with attentiveness [38] and sensory perception [39] and have a strong relation to both cognitive processing and temporal binding of sensory stimuli [40, 41]. These oscillations are found in different brain systems, including the cerebral cortex, hippocampus, and olfactory bulb. Cortical gamma oscillations may become synchronized within 1–2 ms over distances of up to a few millimeters [39] and have been shown to be critical for feature integration in perception and may control the occurrence and polarity of Hebbian modifications. Despite the importance of these processes, the genesis and synchronization mechanisms of fast beta (15–30 Hz) and gamma (30–80 Hz) activities remain poorly understood. In this study, we used computational network models to study basic synaptic mechanisms and properties of fast network oscillations.

7.1 Gamma Oscillations and Synchronization in Small Neuronal Circuits

We first considered a minimal network model consisting of three excitatory (RS type) and one inhibitory (FS type) neuron (Fig. 11, left). The RS neurons produced tonic spiking with random initial phases in the absence of synaptic coupling. Neuronal dynamics was simulated using map-based models implemented with difference equations (maps) for RS and FS cells described in Section 5. The synaptic connections were modeled with equations (6) and (7), where the strength of the individual synapses g_{syn} was scaled by the number of the presynaptic cells. The parameter γ for the excitatory and inhibitory synapses was
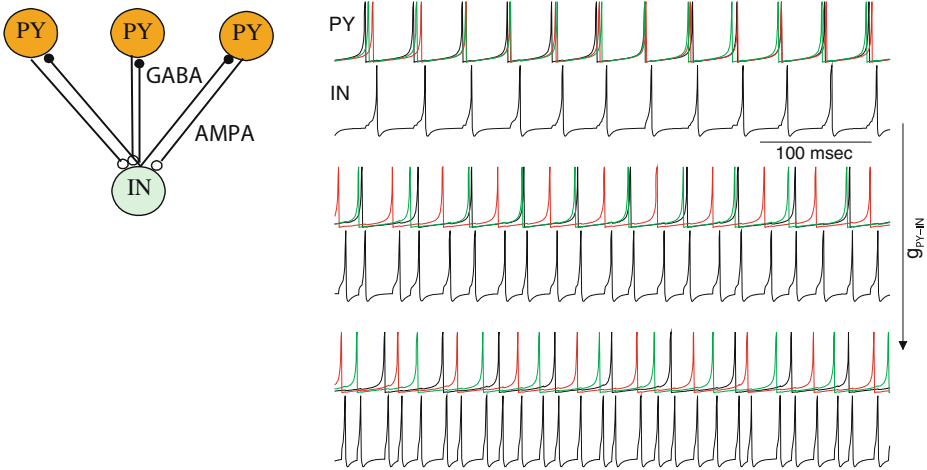
Fig. 11 Oscillations in the model of three PY neurons and one IN. *Left*, excitatory (RS-type) PY neurons are mutually connected with inhibitory (FS-type) IN. *Right*, increase of excitatory input from PY neurons to IN (from *top* to *bottom*) changed the type of oscillations. *Different colors* indicate three different PY neurons

set at $\gamma = 0.4$ and $\gamma = 0.3$, respectively. When excitatory (AMPA-type) connections from pyramidal (PY) neurons to the IN and inhibitory ($GABA_A$-type) connections from IN to PY neurons were introduced, the network oscillations became synchronized in the 20–40-Hz frequency range (Fig. 11, right). The strength of the coupling between IN and PY neurons determined the synchrony and the resonance mode of synchronization. For weak PY–IN coupling, all three PY neurons fired together with minimal jitter. The IN typically fired a few milliseconds later. Increasing the strength of the excitatory input from PY neurons to IN changed the frequency (f) of oscillations and also transformed oscillations from 1/1 resonance mode ($f_{PY} = f_{IN}$) to 1/2 mode ($2f_{PY} = f_{IN}$) and then to 1/3 mode ($3f_{PY} = f_{IN}$) (Fig. 11).

7.2 Synchronization Regimes in Large One-dimensional Network Models

We constructed a large-scale one-dimensional model including layers of excitatory PY and inhibitory IN cells (Fig. 12).

Mean field potential (FP) was estimated as the average of membrane potentials of all PY neurons in the network, and the network activity was characterized by the frequency of the highest peak in the power spectrum of the mean field oscillations. Results of this
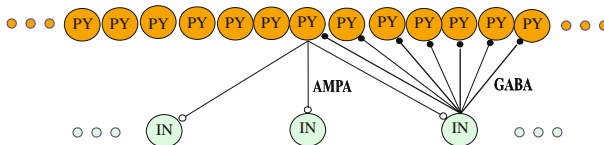

Fig. 12 Sketch of a two-layer network containing RS PY cells and FS INs. The radius of connection footprint was eight neurons (16 presynaptic neurons) for AMPA-type excitatory PY–IN synapses and two neurons (five presynaptic neurons) for $GABA_A$-mediated IN–PY synapses

Fig. 13 Resonance phase locking in one-dimensional network model of 256 PY neurons and 64 IN neurons. Frequency corresponding to the highest peak in the power spectrum of the mean field of PY cells' activity is plotted as a function of synaptic coupling between PY cells and INs. Note several *bands* corresponding to different resonance-locking modes between FP and PY neurons. The ratio f_{PY}/f_{FP} changed from one (*lowest band*) to four (*highest band*)
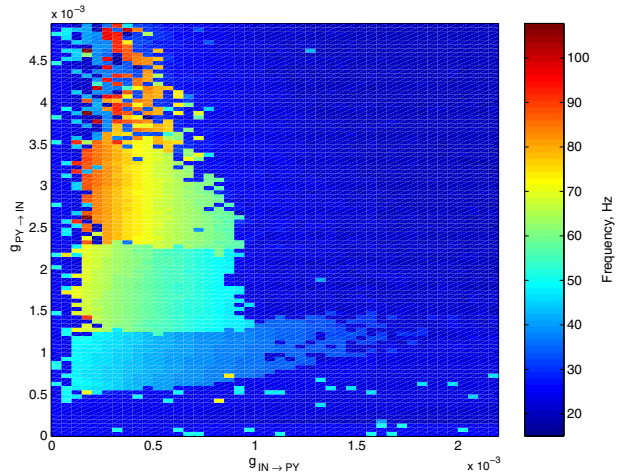
analysis are presented in Figs. 13 and 14. For a large range of synaptic coupling coefficients, the network displayed fast oscillations in the gamma (Fig. 13, left half-plane) or beta (Fig. 13, upper-right corner) frequency ranges. The specific dynamical state of the network varied significantly across the plane of parameters shown in Fig. 13. Consider the ratio (f_{PY}/f_{FP}) of the frequency of a single PY cell oscillation (f_{PY}) to the mean field frequency (f_{FP}). Variations of power spectra corresponding to an increase in PY–IN coupling strength presented in Fig. 14 shows that the different phase-locking modes were altered, changing the frequency ratio in steps. This behavior is consistent with our study of a small neuronal circuit (Fig. 11). Increase of PY–IN coupling was followed by a step-like increase in the mean field frequency (f_{FP}) while the frequency remained almost unchanged between the bifurcation points (Fig. 14, top/left). Also, the frequency of the main harmonic of the PY oscillations (f_{PY}) decreased in the same step-like matter (Fig. 14, middle/left). As a result, the frequency ratio f_{PY}/f_{FP} changed at each bifurcation point $(1/1) \rightarrow (1/2) \rightarrow (1/3)$. The frequency of the IN's oscillations was always equal to the frequency of mean field activity (Fig. 14, bottom/left). When IN–PY coupling was increased, this bifurcation structure disappeared (Fig. 14, right). These results suggest that (1) input from GABAergic INs is critical for synchronizing the network oscillations in the gamma–beta frequency range and (2) the balance between excitatory (PY–IN) and inhibitory (IN–PY) coupling controls the frequency of oscillations and the resonance mode (f_{PY}/f_{FP} ratio).

7.3 Spatiotemporal Properties of Synchronization

Our study predicts that oscillations could be globally synchronized among neurons with different resting potentials and connected with synaptic delays even when each neuron starts its evolution from a different initial condition. An example of this regime is shown in Fig. 15a. Oscillations in different spatial sites were synchronized within a 1–2-ms range while the direct propagation of activity between remote sites would require more than 20 ms. During fast globally synchronized oscillations, the synchrony between PY neurons was mediated by a very fast spread of excitation across INs. Excitatory PY–PY connections were excluded from these simulations. The boundary between already active and still silent IN neurons propagated much faster than synaptic delays would allow, indicating that IN–
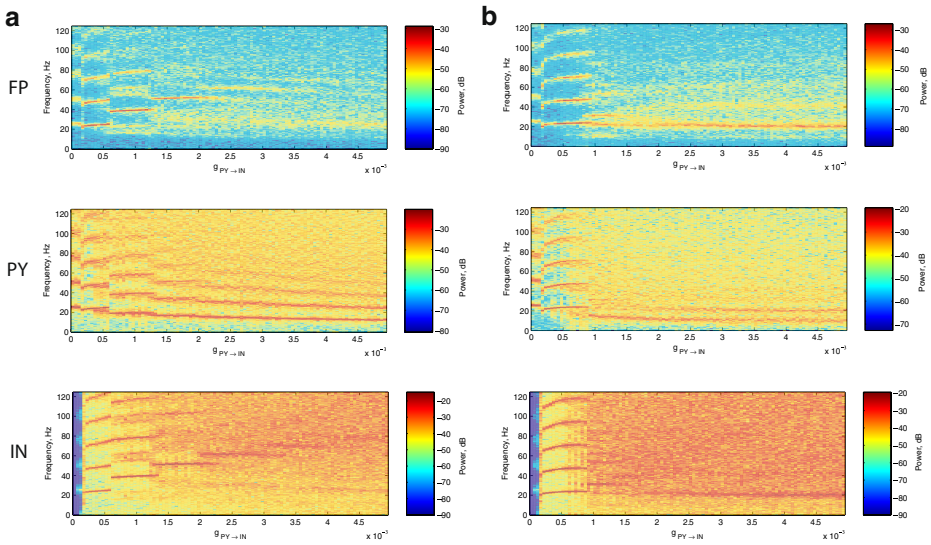
Fig. 14 Spectrograms of oscillation in one-dimensional IN–PY network. Increase of PY–IN coupling was followed by decrease of PY frequency (f_{PY}) and increase of f_{FP} and f_{IN}. Inhibitory INs always fired at the frequency of the FP oscillations. **a** $g_{IN-PY} = 0.0007$. **b** $g_{IN-PY} = 0.0015$

PY–IN synaptic connectivity is not responsible for the direct spread of activity from one group of neurons to another. Instead, synaptic coupling created and maintained a regime of phase synchronization where nearby neurons fire with minimal delays. The phase delay was small even between remote sites. Changing synaptic coupling transformed the globally synchronized state either to a regime of propagating gamma waves (Fig. 15b) or to a regime of asynchronous oscillations (Fig. 15c). The representation of visual objects in the primary visual cortex of awake monkeys has been found to correspond with waves of gamma activity propagating across the cortical surface [42]. It was proposed that the phase continuity of such gamma-waves may be the basis of spatial feature binding across entire objects [43]. Our study suggests that the onset of global synchronization is possible when the network is homogeneous enough—all the synaptic weights and intrinsic parameters of the individual units are selected within the same region of synchronization (see (Fig. 13)). However, when different units belong to different synchronization bands (e.g., when variability between units is large), the network dynamics leads to regimes with activity propagating from one part of the network to another [e.g., in the form of rotating spiral waves (Fig. 15b)]. This creates a finite time lag between oscillations in remote sites (Fig. 15b, bottom).

The study suggests that FS inhibitory INs mediate synchronization of cortical excitatory neurons, creating large areas of stable synchronized network oscillations where excitatory cells are phase-locked to the field at rational frequencies. Changing the strength of inhibitory coupling controls transitions between persistent ($f_{PY}/f_{FP} << 1$) [44] and transient ($f_{PY}/f_{FP} \sim 1$) [45] types of gamma oscillations. Long-range excitatory connections between PY cells are not required for global synchrony. The strength of synaptic interactions between PY cells and INs defines the synchronization state of the network: either global synchronization with near zero phase lag between remote sites (see, e.g., [39]) or local synchrony mediated by waves of gamma activity propagating through the network (see, for example, [42]).
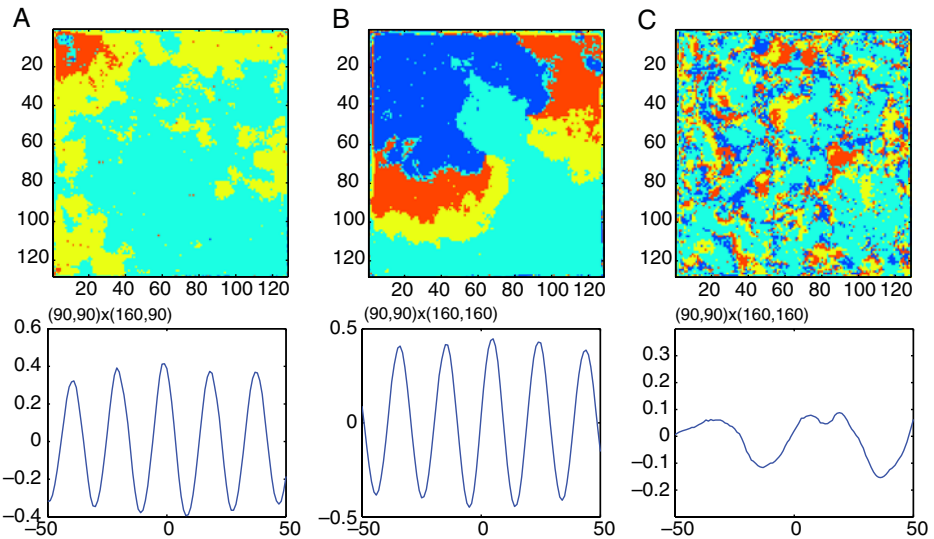
Fig. 15 Oscillations in two-dimensional network model of 256×256 PY neurons and 128×128 INs. Snapshots of activity in inhibitory, IN, population (*top*) and cross correlation of local FPs (average activity of 100×100 PY neurons) between two remote spatial areas (*bottom*) are shown. **a** Nearly global synchronization–phase locking with zero phase shift, $g_{PY-IN}=0.002$, $g_{IN-PY}=0.0007$. **b** Local synchronization mediated by two rotation spiral waves, $g_{PY-IN}=0.0015$, $g_{IN-PY}=0.0007$. **c** Asynchronous state, $g_{PY-IN}=0.002$, $g_{IN-PY}=0.0015$. In *top panels*, *red*, depolarizing (spikes), and *blue*, hyperpolarizing potentials

8 Conclusion

In this manuscript, we presented a complete description of discrete time neuronal models capable of simulating realistic firing patterns of many different classes of biological neurons. Specifically, response patterns of RS, IB, FS, and LTS cortical cells and INs, as well as thalamic relay neurons, have been simulated. For the class of RS neurons, we also showed that complex resonance properties of cortical RS neurons during periodic sinusoidal external stimulation can be correctly captured. Based on the reduced model design, we studied a large-scale cortical network model showing a spectrum of oscillatory states including fast gamma range (30–80 Hz) oscillations. Our approach, combining biological feasibility with high computational efficiency, may be applied to study many biological problems where the size of the network plays an important role. Indeed, there are already a number of studies of neuronal dynamics based on this model [46–51]. The simple mathematical implementation of these models makes them a useful tool for education. These models can be used to illustrate the basics of dynamical mechanisms behind specific forms of firing patterns and network behavior. Finally, the map-based models create new opportunities for the design of real-time systems that reproduce the functionality of real biological networks containing a large number of neurons that can be used in biomimetic robots and other applications.

References

1. Hodgkin, A.L, Huxley, A.F.: A quantitative description of membrane current and its application to conduction and excitation in nerve. J. Physiol. (Lond.) **117**, 500–544 (1952)
2. Bazhenov, M., Timofeev, I., Steriade, M., Sejnowski, T.J.: Model of thalamocortical slow-wave sleep oscillations and transitions to activated states. J. Neurosci. **22**, 8691–8704 (2002)
3. Golomb, D.: Models of neuronal transient synchrony during propagation of activity through neocortical circuitry. J. Neurophysiol. **79**, 1–12 (1998)
4. Golomb, D., Amitai, Y.: Propagating neuronal discharges in neocortical slices: computational and experimental study. J. Neurophysiol. **78**, 1199–1211 (1997)
5. Houweling, A.R., Bazhenov, M., Timofeev, I., Grenier, F., Steriade, M., Sejnowski, T.J.: Frequency-selective augmenting responses by short-term synaptic depression in cat neocortex. J. Physiol. **542**, 599–617 (2002)
6. Mainen, Z.F., Sejnowski, T.J.: Influence of dendritic structure on firing pattern in model neocortical neurons. Nature **382**, 363–366 (1996)
7. Bazhenov, M., Timofeev, I., Steriade, M., Sejnowski, T.: Patterns of spiking-bursting activity in the thalamic reticular nucleus initiate sequences of spindle oscillations in thalamic network. J. Neurophysiol. **84**, 1076–1087 (2000)
8. Bazhenov, M., Timofeev, I., Steriade, M., Sejnowski, T.J.: Computational models of thalamocortical augmenting responses. J. Neurosci. **18**, 6444–6465 (1998)
9. Destexhe, A., Bal, T., McCormick, D.A., Sejnowski, T.J.: Ionic mechanisms underlying synchronized and propagating waves in a model of ferret thalamic slices. J. Neurophysiol. **76**, 2049–2070 (1996)
10. Bazhenov, M., Timofeev, I., Steriade, M., Sejnowski, T.J.: Self-sustained rhythmic activity in the thalamic reticular nucleus mediated by depolarizing GABAA receptor potentials. Nat. Neurosci. **2**, 168–174 (1999)
11. Destexhe, A., Contreras, D., Sejnowski, T.J., Steriade, M.: A model of spindle rhythmicity in the isolated thalamic reticular nucleus. J. Neurophysiol. **72**, 803–818 (1994)
12. Golomb, D., Wang, X.-J., Rinzel, J.: Propagation of spindle waves in a thalamic slice model. J. Neurophysiol. **75**, 750–769 (1996)
13. Traub, R.D., Jefferys, J.G., Whittington, M.A.: Simulation of gamma rhythms in networks of interneurons and pyramidal cells. J. Comput. Neurosci. **4**, 141–150 (1997)
14. Traub, R.D., Whittington, M.A., Colling, S.B., Buzsaki, G., Jefferys, J.G.: Analysis of gamma rhythms in the rat hippocampus in vitro and in vivo. J. Physiol. **493**(Pt. 2), 471–484 (1996)
15. Bazhenov, M., Stopfer, M., Rabinovich, M., Abarbanel, H.D., Sejnowski, T.J., Laurent, G.: Model of cellular and network mechanisms for odor-evoked temporal patterning in the locust antennal lobe. Neuron **30**, 569–581 (2001)
16. Bazhenov, M., Stopfer, M., Rabinovich, M., Huerta, R., Abarbanel, H.D., Sejnowski, T.J., Laurent, G.: Model of transient oscillatory synchronization in the locust antennal lobe. Neuron **30**, 553–567 (2001)
17. Knight, B.W.: Dynamics of encoding in a population of neurons. J. Gen. Physiol. **59**, 734–766 (1972)
18. Stein, R.B.: The frequency of nerve action potentials generated by applied currents. Proc. R. Soc. Lond., B Biol. Sci. **167**, 64–86 (1967)
19. Tuckwell, H.C.: Introduction to Theoretical Neurobiology, vol. 2. Nonlinear and Stochastic Theories. Cambridge University Press, Cambridge (1988)
20. Casti, A.R., Omurtag, A., Sornborger, A., Kaplan, E., Knight, B., Victor, J., Sirovich, L.: A population study of integrate-and-fire-or-burst neurons. Neural Comput. **14**, 957–986 (2002)
21. Smith, G.D., Cox, C.L., Sherman, S.M., Rinzel, J.: Fourier analysis of sinusoidally driven thalamocortical relay neurons and a minimal integrate-and-fire-or-burst model. J. Neurophysiol. **83**, 588–610 (2000)
22. Izhikevich, E.M.: Simple model of spiking neurons. IEEE Trans. Neural Netw. **14**, 1569–1572 (2003)
23. Rulkov, N.F., Timofeev, I., Bazhenov, M.: Oscillations in large-scale cortical networks: map-based model. J. Comput. Neurosci. **17**, 203 (2004)
24. Rulkov, N.F.: Modeling of spiking-bursting neural behavior using two-dimensional map. Phys. Rev. E **65**, 041922 (2002).
25. Bazhenov, M., Rulkov, N.F., Fellous, J.M., Timofeev, I.: Role of network dynamics in shaping spike timing reliability. Phys. Rev. E **72**, 041903 (2005)
26. Shilnikov, A.L., Rulkov, N.F.: Origin of chaos in a two-dimensional map modeling spiking-bursting neural activity. Int. J. Bifurc. Chaos **13**, 3325 (2003).
27. Kuznetsov, Y.A.: Elements of Applied Bifurcation Theory, 3rd edn. Springer, New York (2004)
28. Rinzel, J., Ermentrout, B.: Analysis of neural excitability and oscillations. In: Koch, C., Segev, I. (eds.) Methods in Neural Modeling. From Ions to Networks. MIT, Cambridge (1998)

29. Elson, R.C., Selverston, A.I., Huerta, R., Rulkov, N.F., Rabinovich, M.I., Abarbanel, H.D.I.: Synchronous behavior of two coupled biological neurons. Phys. Rev. Lett. **81**, 5692 (1998)
30. Selverston, A.I.: Structural and functional basis of motor pattern generation in the stomatogastric ganglion of the lobster. Am. Zool. **14**, 957 (1974)
31. Protopapas, A.D., Vanier, M., Bower, J.M.: Simulating of lagre networks of neurons. In: Koch, Ch., Segev, I. (eds.) Methods in Neuronal Modeling: from Ions to Networks, p. 461. MIT, Cambridge (1998)
32. Bacci, A., Rudolph, U., Huguenard, J.R., Prince, D.A.: Major differences in inhibitory synaptic transmission onto two neocortical interneuron subclasses. J. Neurosci. **23**(29), 9664–9674 (2003)
33. McCormick, D.A., Pape, H.C.: Properties of a hyperpolarization-activated cation current and its role in rhythmic oscillation in thalamic relay neurones. J. Physiol. **431**, 291–318 (1990)
34. Nuñez, A., Amzica, F., Steriade, M.: Electrophysiology of cat association cortical cells in vitro: intrinsic properies and synaptic responses. J. Neurophysiol. **70**, 418–430 (1993)
35. Timofeev, I., Bazhenov, M.: In: Columbus, F. (ed.) Trends in Chronobiology Research, pp. 1–47. Nova, Commack (2005)
36. Fellous, J.M., Houweling, A.R., Modi, R.H., Rao, R.P., Tiesinga, P.H., Sejnowski, T.J.: Frequency dependence of spike timing reliability in cortical pyramidal cells and interneurons. J. Neurophysiol. **85**, 1782–1787 (2001)
37. Schreiber, S., Fellous, J.M., Tiesinga, P., Sejnowski, T.J.: Influence of ionic conductances on spike timing reliability of cortical neurons for suprathreshold rhythmic inputs. J. Neurophysiol. **91**, 194–205 (2004)
38. Rougeul-Buser, A., Bouyer, J.J., Buser, P.: From attentiveness to sleep. A topographical analysis of localized "synchronized" activities on the cortex of normal cat and monkey. Acta Neurobiol. Exp. (Warsz) **35**, 805–819 (1975)
39. Gray, C.M., Konig, P., Engel, A.K., Singer, W.: Oscillatory responses in cat visual cortex exhibit intercolumnar synchronization which reflects global stimulus properties. Nature **338**, 334–337 (1989)
40. Llinas, R., Ribary, U.: Coherent 40-Hz oscillation characterizes dream state in humans. Proc. Natl. Acad. Sci. U. S. A. **90**, 2078–2081 (1993)
41. Singer, W., Gray, C.M.: Visual feature integration and the temporal correlation hypothesis. Annu. Rev. Neurosci. **18**, 555–586 (1995)
42. Gabriel, A., Eckhorn, R.: A multi-channel correlation method detects traveling gamma-waves in monkey visual cortex. J. Neurosci. Methods **131**, 171–184 (2003)
43. Eckhorn, R., Gail, A., Bruns, A., Gabriel, A., Al-Shaikhli, B., Saam, M.: Neural mechanisms of visual associative processing. Acta Neurobiol. Exp. (Wars) **64**, 239–252 (2004)
44. Buhl, E.H., Tamas, G., Fisahn, A.: Cholinergic activation and tonic excitation induce persistent gamma oscillations in mouse somatosensory cortex in vitro. J. Physiol. (Lond.) **513**, 117–126 (1998)
45. Whittington, M.A., Stanford, I.M., Colling, S.B., Jefferys, J.G., Traub, R.D.: Spatiotemporal patterns of gamma frequency oscillations tetanically induced in the rat hippocampal slice. J. Physiol. **502**(Pt. 3), 591–607 (1997)
46. Casado, J.M.: Transient activation in a network of coupled map neurons. Phys. Rev. Lett. **91**, 208102 (2003)
47. Casado, J.M., Ibarz, B., Sanjuan, M.A.F.: Winnerless competition in networks of coupled map neurons. Mod. Phys. Lett. B **18**, 1347–1366 (2004)
48. Ivanchenko, M.V., Osipov, G.V., Shalfeev, V.D., Kurths, J.: Synchronized bursts following instability of synchronous spiking in chaotic neuronal networks. Los Alamos National Laboratory, Los Alamos, nlin.CD/0601023 (2006)
49. Nowotny, T., Huerta, R., Abarbanel, H.D., Rabinovich, M.I.: Self-organization in the olfactory system: one shot odor recognition in insects. Biol. Cybern. **93**, 436–446 (2005)
50. Osipov, G.V., Ivanchenko, M.V., Kurths, J., Hu, B.: Synchronized chaotic intermittent and spiking behavior in coupled map chains. Phys. Rev. E **71**, 056209 (2005)
51. Assisi, C., Stopfer, M., Laurent, G., Bazhenov, M.: Adaptive regulation of sparseness by feedforward inhibition. Nat. Neurosci. **10**(9), 1176–1184 (2007)